IEEE Access
Multidisciplinary ⋮ Rapid Review ⋮ Open Access Journal

Received 1 June 2024, accepted 13 June 2024, date of publication 19 June 2024, date of current version 27 June 2024.

Digital Object Identifier 10.1109/ACCESS.2024.3416473

RESEARCH ARTICLE

Enhanced Dual-Vector Model Predictive Current Integrated Control for Electric-Drive-Reconstructed Onboard Chargers

FENG YU, (Member, IEEE), QIHAO YIN, LAIWU LUO, AND YUHAO ZHANG
School of Electrical Engineering and Automation, Nantong University, Nantong 226019, China

Corresponding author: Laiwu Luo (luolaiwu@ntu.edu.cn)

This work was supported in part by the National Natural Science Foundation of China under Grant 52177051; in part by the Excellent Young Backbone Teacher of "Qinglan Project" of Jiangsu Colleges and Universities, in 2022; and in part by the Postgraduate Research and Practice Innovation Program of Jiangsu Province under Grant KYCX24_3575.

ABSTRACT Electric-drive-reconstructed on-board chargers (EDROCs) have emerged as a viable solution to alleviate mileage anxiety in electric vehicles (EVs) over the past decade. Nevertheless, the inclusion of additional components and separate control strategies in the previous EDROCs undeniably results in an escalation of system cost and control complexity. To address such an issue, an enhanced dual-vector model predictive current integrated control (MPCIC) for EDROCs is proposed, which is designed for the solar-powered electric vehicle (SPEV) that is equipped with a symmetrical six-phase machine. Firstly, the proposed topology implements the integration of charging and driving operations by re-leveraging the inherent traction system, significantly minimizing the incremental components. Secondly, the integrated control strategy for all operation modes is devised by incorporating the enhanced dual-vector model predictive control (MPC), mitigating the complexities and enhancing reliability. In this enhanced MPC, 12 virtual vectors, which consist of two active vectors, along with the optimized cost function are introduced, effectively suppressing harmonic currents. To this end, the effectiveness of the proposed EDROC is verified through a 2-kW experimental prototype under different operation modes.

INDEX TERMS Electric-drive-reconstructed on-board charger, model predictive current integrated control (MPCIC), solar-powered electric vehicle (SPEV), six-phase machine drive.

I. INTRODUCTION

With the escalating environmental concerns arising from industrial pollution, electric vehicles (EVs) have recently garnered significant attention as a potential mode of transportation [1]. The advancement of EVs has propelled the progress of associated technologies, such as propulsion and battery charging. Nevertheless, the further popularization of EVs is hindered by concerns about limited mileage and restricted charging due to insufficient charging facilities. Consequently, the development of on-board charging technology in EVs holds great practical significance for promoting EVs [2], [3], [4]. The on-board charger (OBC), which has a lower price and higher convenience compared to the off-board charger, has matured over the past decade. In particular, the electric-drive-reconstructed onboard charger (EDROC) provides a new lightweight design concept for the electric component of EVs, aiming to utilize electric drive units to perform driving and charging operations separately at different moments [5]. As such, a significant amount of effort has been dedicated to researching the topological and performance of the EDROC [6], [7], [8].

The EDROC system encompasses various types of motors, which are classified based on the number of phases utilized for motor reusability and can be categorized as either three or multi-phase. Notably, the EDROC system, which was initially employed in 1985 [9], is based on a three-phase motor and utilized for achieving single-phase charging. However,

The associate editor coordinating the review of this manuscript and approving it for publication was Zhong Wu.

the system of EVs based on multi-phase machines, takes some merits over three-phase counterparts, especially owing to the smooth torque generation, extra control degrees of freedom, and excellent fault tolerance capacity [10], [11]. Therefore, the multiphase machine has garnered significant applications in several EV enterprises, such as the SUMO series of DANA TM4 company [12]. A significant number of multiphase EDROCs are successively reported based on the application of multiphase machines [13], [14], [15]. In [13], an exploration of the single-phase charging EDROC system utilizing a five-phase machine is presented. Referring to the [14], two charging configurations of the EDROC system connecting to a three-phase grid are proposed, incorporating symmetrical and asymmetrical six-phase machines. Additionally, the EDROC system based on nine-phase machine is investigated in [15], capable of facilitating both three-phase and single-phase charging.

In addition to the aforementioned EDROCs powered by grids, an alternative EDROC powered by vehicle-roof photovoltaic panels (VRPPs) has garnered significant attention for solar-powered EVs (SPEVs) that are both environmentally friendly and capable of extended mileage range [16]. However, the conventional EDROC system necessitates additional components in SPEVs, undoubtedly increasing both the cost and the complexity of control [17]. Catered to the requirement of SPEVs, an inventive EDORC system for SPEVs incorporating six-phase machine is presented in [18] with the functions of in-motion charging (charging and driving simultaneously) and DC charging. It utilizes the spatial degrees of freedom of the multiphase machine without additional power components. Nevertheless, the control strategies for driving and charging are designed separately, resulting in increased design costs and control complexity. To address this issue, a multi-energy interface EDROC is presented in [19], incorporating the functions of in-motion charging, single-phase charging and DC charging by the integrated control strategy. This further substantiates the viability of integrated software control within multi-phase EDROC systems.

Intrinsically, the control strategy for software integration can be fulfilled by harnessing the features of multiphase machines, as demonstrated in the proposed topologies of [18] and [19], where battery charging is implemented by regulating the 0-axis current. However, when the 0-axis current control is extended to the drive system, an additional current proportional-integral (PI) controller must be involved to tackle the 0-axis current. The utilization of multiple subspace PI current controllers in vector control strategy complicates the tuning process for the PI parameters. Comparatively, model predictive control (MPC) takes several advantages of the high dynamic performance, feasible implementation for multi-objective control and easy integration of nonlinear constraints, emerging as efficacious remedies to tackle the aforementioned concerns. Currently, it has been successfully investigated in the new energy conversion system [20], [21], drive systems [22], [23] and EDROC systems [24], [25], [26]. In [24], the effectiveness of MPC in controlling the symmetrical six-phase EDROC during both propulsion and charging modes has been demonstrated. The three-phase grid currents are directly regulated by reconfiguring the six-phase stator winding into an equivalent three-phase winding in the charging mode. However, the maximum charging power is restricted to half of the propulsion power. To tackle the issue of low charging power, [25] explores the MPC scheme and maximum charging power of a six-phase EDROC in three-phase charging mode with three different winding configurations. However, the inclusion of sequence current control in the system introduces additional constraints to the cost function, thereby posing difficulties in the design of the weight factors. In summaries, the investigation of software integration for driving and charging modes by the MPC scheme is insufficient thus far.

Recently, the MPC scheme of six-phase EDROC system under single-phase charging process with three different winding configurations was investigated in [26], and the regulation of the 0-axis current component was utilized for implementing battery charging. On this basis, the normal driving function is maintained when MPC is utilized in charging mode, enabling independent control over the charging and driving components. Crucially, the research of the MPC scheme for EDROC systems implies that the integration of driving and charging control strategies can be achieved by leveraging the benefits of multi-objective control.

According to the previous research and methodologies, an enhanced dual-vector model predictive current integrated control for EDROC is proposed for the SPEV equipped with a six-phase machine, as shown in Fig. 1. The topology ingeniously combines the functionalities of DC charging, in-motion charging, and normal driving. In terms of the studied EDROC, three primary contributions are indicated, as follows:

1) Diverging from the conventional reliance on charging station-dependent EVs, the integration of VRPPs and DC grids into the EDROC enhances charging convenience and extends the mileage range of SPEVs.
2) Compared to a standard OBC, the integration of VRPPs into the EDROC eliminates the necessity for additional DC/DC converter and only two mode switches and voltage sensors are installed, resulting in a more cost-effective, compact, and reliable charger.
3) To address the issue of separate design of control strategies for driving and charging in existing research, an enhanced dual-vector model predictive current integrated control (MPCIC) is employed to seamlessly integrate these functions, resulting in a more streamlined and reliable approach. Furthermore, this work investigates optimal voltage vectors and cost function for the MPCIC to effectively suppress harmonic currents and enhance control accuracy.

The rest of this paper is organized as follows. Firstly, the operation modes and principles of the studied EDROC are discussed exhaustively in Section II. Secondly, the basic principles of the conventional MPC and the enhanced dual-vector

MPC are investigated in Section III. After that, the implementation process of mode integrated control is proposed. Then, to verify the steady-state and dynamic behavior of the proposed EDROC system under different operation scenarios, a 2-kW experimental test rig is conducted in Section IV. Finally, the conclusions are given in Section V.

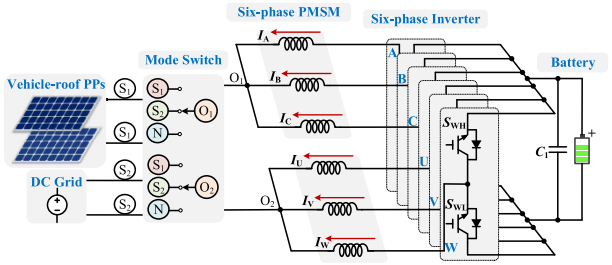

FIGURE 1. The proposed topology of the EDROC.

II. TOPOLOGY AND OPERATION MODES

The topology of the EDROC is composed of a symmetrical six-phase PMSM with two available neutral points, a battery, a six-phase two-level inverter, a set of VRPPs, a digital control system, two mode switches (S_1, S_2), as shown in Fig.1. According to the energy input interfaces, the system possesses three operation modes: (1) normal driving mode; (2) DC charging mode; and (3) in-motion charging mode. The analysis of the DC charging and the in-motion charging modes will be discussed in detail in the following part (see Section II-B).

A. MATHEMATICAL MODEL OF SIX-PHASE PMSM

Considering the inherent characteristics of nonlinearity and strong coupling, the analysis and control of six-phase PMSM are commonly simplified by utilizing the vector space decomposition (VSD) approach [27]. By this approach, the voltage and the current vectors are mapped into three orthogonal subspaces, namely α–β, x–y, and 0_1–0_2 subspaces. On the basis of the amplitude invariance criterion, the decoupling matrix $\mathbf{T}_{\mathrm{VSD}}$ and the Park transformation matrix $\mathbf{T}_{\mathrm{Park}}$ are expressed as

$$\mathbf{T}_{\mathrm{VSD}} = \frac{1}{3}\begin{bmatrix} 1 & 1/2 & -1/2 & -1 & -1/2 & 1/2 \\ 0 & \sqrt{3}/2 & \sqrt{3}/2 & 0 & -\sqrt{3}/2 & -\sqrt{3}/2 \\ 1 & -1/2 & -1/2 & 1 & -1/2 & -1/2 \\ 0 & \sqrt{3}/2 & -\sqrt{3}/2 & 0 & \sqrt{3}/2 & -\sqrt{3}/2 \\ 1/2 & -1/2 & 1/2 & -1/2 & 1/2 & -1/2 \\ 1/2 & 1/2 & 1/2 & 1/2 & 1/2 & 1/2 \end{bmatrix} \tag{1}$$

$$\mathbf{T}_{\mathrm{Park}} = \begin{bmatrix} \cos\theta_e & \sin\theta_e \\ -\sin\theta_e & \cos\theta_e \end{bmatrix} \tag{2}$$

where θ_e signifies the electrical angular.

From the three orthogonal subspaces, the α–β subspace plays a crucial role in conversion of electromechanical energy, while the x–y subspace is responsible for mapping the harmonics that only result in losses and ideally should be minimized. Additionally, the components of the 0_1- and 0_2- axes are constantly zero in case of isolated neutral points. By utilizing the matrix $\mathbf{T}_{\mathrm{VSD}}$ and the $\mathbf{T}_{\mathrm{park}}$, the subspace voltages can be described as

$$\begin{bmatrix} u_d \\ u_q \end{bmatrix} = \begin{bmatrix} R_s & -\omega_e L_q \\ \omega_e L_d & R_s \end{bmatrix}\begin{bmatrix} i_d \\ i_q \end{bmatrix} + \begin{bmatrix} L_d & 0 \\ 0 & L_q \end{bmatrix}\frac{d}{dt}\begin{bmatrix} i_d \\ i_q \end{bmatrix} + \begin{bmatrix} 0 \\ \psi_f \end{bmatrix} \tag{3}$$

$$\begin{bmatrix} u_x \\ u_y \end{bmatrix} = R_s\begin{bmatrix} i_x \\ i_y \end{bmatrix} + L_\sigma\frac{d}{dt}\begin{bmatrix} i_x \\ i_y \end{bmatrix} \tag{4}$$

$$\begin{bmatrix} u_{01} \\ u_{02} \end{bmatrix} = R_s\begin{bmatrix} i_{01} \\ i_{02} \end{bmatrix} + L_\sigma\frac{d}{dt}\begin{bmatrix} i_{01} \\ i_{02} \end{bmatrix} \tag{5}$$

where u_k ($k \in \{d, q, x, y, 0_1, 0_2\}$) is the voltage of k-axis, while i_k is the current of k-axis; L_d, L_q, and L_σ are d-axis, q-axis and the stator leakage inductances, respectively; R_s is the stator resistance; ω_e is the electrical angular speed; ψ_f is the permanent magnet flux. The electromagnetic torque can be expressed as

$$T_e = 3p_n i_q\left(i_d\left(L_d - L_q\right) + \psi_f\right) \tag{6}$$

where p_n is the number of pole pairs.

B. OPERATION PRINCIPLE ANALYSIS

1) NORMAL DRIVING MODE

The normal driving mode, extensively discussed in numerous articles on multi-phase motor drives, has been described in detail. In this operating mode, the two available neutral points are in the open position (position N), and a six-phase inverter is utilized to drive the six-phase PMSM. Simultaneously, the battery serves as the sole energy source.

From the control perspective, (6) demonstrates that the output torque of the six-phase PMSM can be modulated by manipulating the d–q subspace currents to achieve speed regulation. Therefore, the control of the six-phase PMSM drive typically involves speed control along with the control of the d–q and the x–y subspace currents. It is unnecessary to adjust the current of the 0_1-axis in this mode.

2) DC CHARGING MODE

When the EV is in idle state, the DC charging mode can be activated by positioning two neutral points of six-phase PMSM at either S_1 to connect the VRPPs or S_2 to connect the DC grid. To simplify the analysis, the assumption is made that the equivalent inductance and resistance of each machine winding are equal. On the basis of that, the equivalent circuit of the system is shown in Fig. 2(a), where the subscript $M \in \{\mathrm{A}, \mathrm{B}, \mathrm{C}\}$ and subscript $N \in \{\mathrm{U}, \mathrm{V}, \mathrm{W}\}$. Furthermore, due to the OFF state of S_{MH} and S_{NL}, the equivalent circuit can be simplified, as shown in Fig. 2(b). Importantly, a six-phase inverter along with a six-phase PMSM is employed as

two boost converts with MPPT capability to regulate either VRPPs or DC grid voltage to the desired charging level.

The DC charging mode encompasses four states since the switches S_{YH} and S_{XL} can be toggled between ON and OFF positions [18]. In each state, the equivalent inductances of the boost converter are either discharged or charged. Therefore, the charging voltage V_b can be controlled by the duty cycle of the switching device in a steady-state and continuous conduction mode based on Kirchhoff's voltage law and volt-second balance principle.

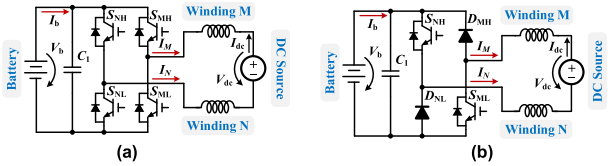

FIGURE 2. (a) Equivalent system circuit in DC charging mode. (b) Simplified circuit in DC charging mode.

In view of the DC charging control, the charging control and subspace currents control methods are utilized in the proposed EDROC. The generation of the zero electromagnetic torque can be controlled by the d-q and the x-y axes currents, while the charging power can be regulated by the 0_1-axis current. Exhaustively, the 0_1-axis current is manipulated to facilitate battery charging current when the DC grid is employed or achieve MPPT when VRPPs are utilized. Due to the spatial freedom of the multi-phase machine and the independent control of subspace currents, it is feasible to implement DC charging by controlling the 0_1-axis current.

3) IN-MOTION CHARGING MODE

During the in-motion charging mode, the connection between the neutral points only involves the VRPPs, and the equivalent circuit is similar to the DC charging mode. The proposed EDROC has the dual purpose of driving the six-phase PMSM and charging the battery via the VRPPs. In terms of source-load characteristics, the VRPPs function as the input power source, while the automotive mechanical load acts as the power-consuming load. Concurrently, the power battery exhibits a unique dual attribute of both a source and a load, depending on the power generation of VRPPs.

Considering the weather variations, the voltage and current of the VRPPs dynamically change in in-motion charging mode. Therefore, according to the operational conditions, the system can function effectively under both abundant and insufficient illumination, indicating that the power generated by the VRPPs is responsible not only for driving but also for charging the battery. The power distribution, as illustrated in Fig. 3, is contingent upon the comparison between the output power of the VRPPs P_{PP} and the electromechanical power P_m. On the one hand, in the case of $P_{PP} > P_m$ (see Fig. 3(a)), the VRPPs independently provide energy to meet the drive requirements, while the surplus energy is directed towards charging the battery, exhibiting the load attribute of the power battery. Conversely, in scenarios where $P_{PP} < P_m$ (see Fig. 3(b)), the system is powered by the battery and the VRPPs, manifesting the source attribute of the power battery.

According to the VSD, the variables in the d-q subspace, the x-y subspace, and the 0_1-axis are mutually decoupled, allowing for independent control of each subspace. Subsequently, the output power of VRPPs can be regulated by the 0_1-axis current to achieve the MPPT purpose. The driving system, which is unrelated to the 0_1-axis current control, can be regulated by the d-q axes current control. Notably, the dedicated DC-DC converter between the VRPPs and the battery is eliminated due to the implementation of the 0_1-axis current control, which effectively decreases the cost associated with system software and hardware design.

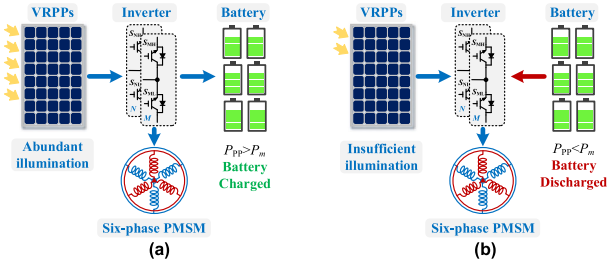

FIGURE 3. Power distribution in in-motion charging mode (a) Battery charged. (b) Battery discharged.

III. CONTROL METHODS DESIGN

Considering the requirements of regulating multiple subspace currents for the aforementioned operating modes described above, the MPC scheme has been validated as a viable approach due to its versatility and multi-objective control. Consequently, an enhanced dual-vector MPCIC is proposed in this section. The proposed MPCIC leverages virtual vectors to alleviate the concerns associated with computational burden in contrast to conventional MPC. Moreover, the software integration of multi-operational modes of control can be realized, effectively streamlining the control process and bolstering the reliability of the system.

A. CONVENTIONAL MPC SCHEME

For the topology of the proposed EDROC, the six-phase two-level inverter has $2^6 = 64$ different switching states. Each switching state combination corresponds to a voltage vector in the α–β and x–y subspace. All vectors can be calculated by

$$\begin{cases} V_{\alpha-\beta} = \dfrac{1}{3}U_{dc}(S_A + S_U m + S_B m^2 + S_V m^3 + S_C m^4 \\ \qquad +S_W m^5) \\ V_{x-y} = \dfrac{1}{3}U_{dc}(S_A + S_U m^2 + S_B m^4 + S_V m^6 + S_C m^8 \\ \qquad +S_W m^{10}) \end{cases} \tag{7}$$

where $m = e^{j60^\circ}$; $S_i (i = A, B, C, U, V, W) \in \{0,1\}$ and represents the switching state of each leg; U_{dc} is the DC bus voltage.

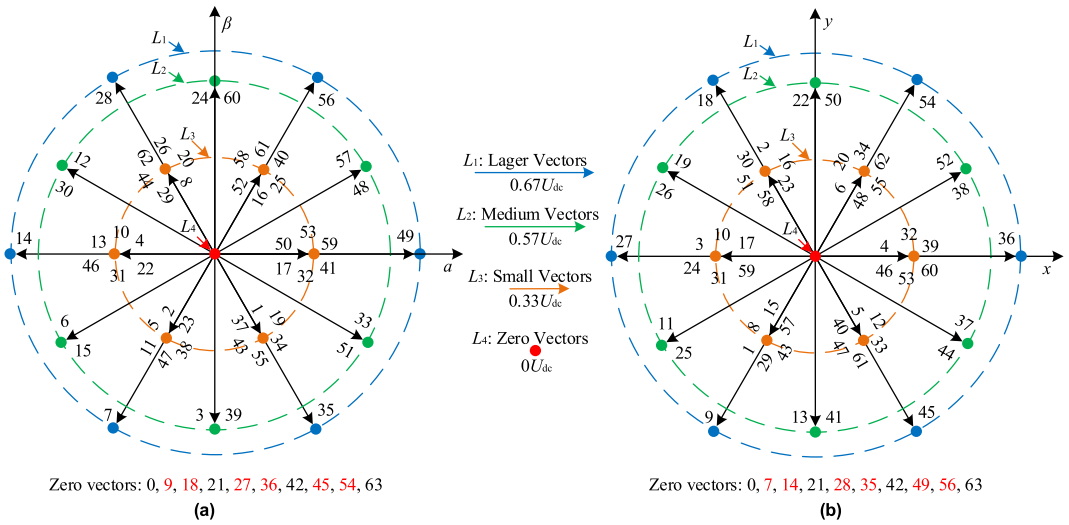

FIGURE 4. Voltage vector mapping for conventional two-level VSI for symmetrical six-phase. (a) $\alpha - \beta$ subspace. (b) x - y subspace.

The vectors that map to different subspaces are determined by the states of the inverter. Specifically, each switch leg of the six-phase inverter has two states, 1 and 0, which correspond to closing the upper and the lower switches, respectively. Therefore, all the vectors can be divided into four categories according to the amplitude of vectors, namely the large vectors L_1 ($0.67U_{dc}$), medium vectors L_2($0.57U_{dc}$), small vectors L_3 ($0.33U_{dc}$), and zero vectors L_4 ($0U_{dc}$), which are represented in the stationary reference in Fig. 4(a)-(b). In general, the larger vectors of α–β subspace are employed expectantly due to the high utilization of DC bus voltage and zero content in the x–y subspace, as shown in Table 1.

TABLE 1. Amplitude of voltage vectors on subspace.

Voltage vectors	α–β subspace	x–y subspace
Large	0.67 U_{dc}	0 U_{dc}
Medium	0.57 U_{dc}	0.57 or 0.33 U_{dc}
Small	0.33 U_{dc}	0.57 or 0.33 U_{dc}
Zero	0 U_{dc}	0.67 or 0 U_{dc}

With the forward Euler discretization method, the predictive mode of the six-phase PMSM can be obtained from (3) and (4), which can be used to predict the current at instant $k+1$. Therefore, the prediction is computed as follows.

$$\begin{cases} i_d(k+1) = \dfrac{T_s}{L_d}u_d(k) + (1 - \dfrac{R_s}{L_d}T_s)i_d(k) + T_s\omega_e\dfrac{L_q}{L_d}i_q(k) \\ i_q(k+1) = \dfrac{T_s}{L_q}u_q(k) + (1 - \dfrac{R_s}{L_q}T_s)i_q(k) - T_s\omega_e\dfrac{L_d}{L_q}i_d(k) \\ \quad - \dfrac{T_s\omega_e\psi_f}{L_q} \end{cases} \tag{8}$$

$$\begin{cases} i_x(k+1) = \dfrac{T_s}{L_\sigma}u_x(k) + (1 - \dfrac{R_s}{L_\sigma}T_s)i_x(k) \\ i_y(k+1) = \dfrac{T_s}{L_\sigma}u_x(k) + (1 - \dfrac{R_s}{L_\sigma}T_s)i_y(k) \end{cases} \tag{9}$$

where T_s is the sampling time; $i_j(k)$ ($j = d, q, x, y$) is the detection value at instant k; $i_j(k+1)$ is the predicted current of j-axis at instant $k+1$.

The optimum switching state is selected by minimizing the cost function. The primary objective of the conventional MPC scheme is to simultaneously track the current references in both α–β and x–y subspace. Hence, the cost function is expressed as

$$J = \left|i_d^* - i_d(k+1)\right| + \left|i_q^* - i_q(k+1)\right| + \lambda_1(|i_x(k+1)| + \left|i_y(k+1)\right|) \tag{10}$$

where i_d^* and i_q^* are the reference currents of d-axis, q-axis; λ_1 is the weighting factor.

The (8)-(10) presented the conventional MPC control in the normal driving mode. However, for the proposed DC charging or in-motion charging modes, additional subspace control is necessary due to the utilization of the 0_1-axis component for battery charging and MPPT purposes.

Accordingly, (5) is discretized, yielding the following equation for predicting the 0_1-axis current

$$i_{01}(k+1) = \frac{T_s}{L_\sigma}u_{01}(k) + (1 - \frac{R_s}{L_\sigma}T_s)i_{01}(k) \tag{11}$$

where $i_{01}(k+1)$ is the predicted current of 0_1-axis at instant $k+1$.

The cost function also varies under the DC charging or in-motion charging mode

$$J = \left|i_d^* - i_d(k+1)\right| + \left|i_q^* - i_q(k+1)\right| + \lambda_1(|i_x(k+1)| + \left|i_y(k+1)\right|) + \lambda_2\left|i_{01}^* - i_{01}(k+1)\right| \tag{12}$$

where λ_2 is the weighting factor; i_{01}^* is the reference current of 0_1-axis.

The ergodic optimization method is widely employed to ascertain the optimal switching state in conventional MPC. Specifically, the predicted currents of the 64 voltage vectors at instant $k+1$ are calculated via the utilization of (8), (9) and (11). Subsequently, according to the ergodic optimization method, the reference and predicted currents are substituted into equation (12) to obtain the optimal voltage vector that minimizes the cost function value. Finally, the switch state corresponding to the optimal vector is utilized as the control action of the subsequent cycles. Nonetheless, this conventional MPC method engenders a significant computational overhead due to the iterative evaluation of all 64 vectors within each period. Additionally, the inclusion of the corresponding weighting factor is also essential. Hence, it is imperative to substantially reduce the computational burden and omit harmonics control of current in order to ensure the targeted driving and charging efficiency. The adoption of the conventional MPC scheme is impracticable for the proposed EDROC.

B. ENHANCED MPC SCHEME

In view of the aforementioned issues, an enhanced MPC scheme by optimizing the voltage vectors is proposed. The enhanced MPC scheme incorporates basic vector reselection and space vector synthetization to address the difficulty of weighting factors and computational burdens.

1) SPACE VECTOR SYNTHETIZATION

For the conventional MPC scheme, 64 basic voltage vectors are utilized during the three operation modes. It is observed that the projection of variables onto the x–y subspace has a substantial impact on the performance. To address this concern, the selection principle of basic vectors can be comprehended as a positive vector operating solely within the fundamental subspace, while the corresponding value is zero in the x–y subspace. For this purpose, the analysis of the voltage vectors in the α–β and the x–y subspace is essential. As illustrated in Table 2, the large vectors in the α–β subspace transform zero vectors within the x–y subspace. Considering the potential impact on the overall control precision of relying exclusively on large vectors as fundamental vectors, utilizing the medium vectors L_2 and small vectors L_3 vectors to synthesize virtual vectors without projection in the x–y subspace is a viable solution.

TABLE 2. Voltage vectors on subspace and zero-sequence voltage.

Voltage vectors	α–β subspace	x–y subspace	0_1 axis
V_{49}	$0.67U_{dc}\,e^{j0}$	0	-0.167 U_{dc}
V_{56}	$0.67U_{dc}\,e^{j(\pi/3)}$	0	0.167 U_{dc}
V_{28}	$0.67U_{dc}\,e^{j(2\pi/3)}$	0	-0.167 U_{dc}
V_{14}	$0.67U_{dc}\,e^{j(\pi)}$	0	0.167 U_{dc}
V_7	$0.67U_{dc}\,e^{j(4\pi/3)}$	0	-0.167 U_{dc}
V_{35}	$0.67U_{dc}\,e^{j(5\pi/3)}$	0	0.167 U_{dc}

On the basis of the virtual vectors, the operating range of the control voltage vectors can be expanded. Therefore, 12 virtual vectors (VVs) are synthesized to guarantee a zero projection in the x–y subspace. According to Fig. 4, each medium vector L_2 has two switching states in the α–β subspace, which undergoes reverse mapping to the x–y subspace. Virtual vectors (VV_1-VV_6) are devised based on the properties of the medium vectors. Specifically, each voltage vector has an equal duration of application, ensuring that the average value of the x–y subspace components remains at zero within a sampling period. Similarly, synthetic vectors for small vectors (VV_7-VV_{12}) are also devised. The formation of the VV_1-VV_{12} is illustrated in Table 3 and visually represented in Fig. 5.

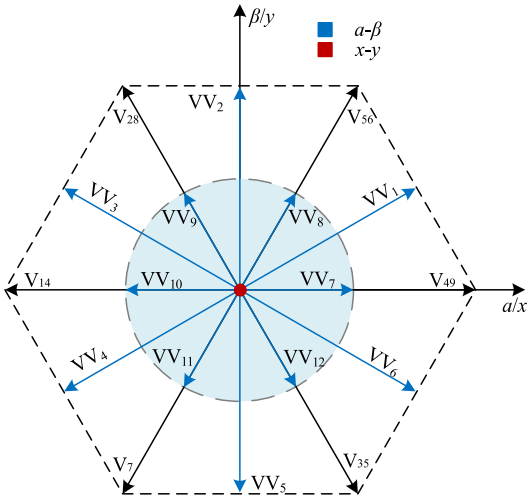

FIGURE 5. Modulated voltage vectors.

TABLE 3. Formation of synthetic voltage vectors.

Virtual vectors	Voltage vectors combination	Virtual vectors	Voltage vectors combination
VV_1	(V_{48}, V_{57})	VV_7	(V_{32}, V_{59})
VV_2	(V_{24}, V_{60})	VV_8	(V_{40}, V_{58})
VV_3	(V_{12}, V_{30})	VV_9	(V_8, V_{62})
VV_4	(V_6, V_{15})	VV_{10}	(V_{10}, V_{46})
VV_5	(V_3, V_{39})	VV_{11}	(V_2, V_{47})
VV_6	(V_{33}, V_{51})	VV_{12}	(V_{34}, V_{43})

Taking vectors V_{48} and V_{57} as exemplification, the duration time can be expressed by

$$\begin{cases} T_1 \times |V_{48}| = T_2 \times |V_{57}| \\ T_1 = T_2 = 0.5T_S \end{cases} \tag{13}$$

where T_1 is the duration time of V_{48}, T_2 is the duration time of V_{57}.

The operational capacity of the motor can be expanded at high speeds by employing the 6 longest magnitudes (large vectors L_1) voltage vectors and 12 virtual vectors to regulate the subspace currents. Meanwhile, the applied voltage vectors exclusively have components only in α–β subspace and 0_1-axis.

In the enhanced dual-vector MPC, 19 vectors are employed to predict the value of the subspace current. Simultaneously, the current prediction results in the x–y subspace can be stored since there are no components in the x–y subspace. The cost function can be simplified as

$$J = \left|i_d^* - i_d(k+1)\right| + \left|i_q^* - i_q(k+1)\right| + \lambda_2 \left|i_{01}^* - i_{01}(k+1)\right| \tag{14}$$

where the λ_2 is equal to 0 in normal driving mode, while the λ_2 is equal to 1 in charging modes (DC charging and in-motion charging modes).

2) DELAY COMPENSATION

The updating process occurs instantaneously and without delay within the control cycle in the ideal discrete-time system. All algorithm calculations and resultant control variable outputs are promptly accomplished during a single control cycle. Nevertheless, the real-time updating of control variable outputs within a single control cycle is impeded due to the requisite time consumed by A/D sampling conversion and algorithm calculations in the practical implementation, which can deteriorate the control performance. A valid solution is using a two-step prediction to compensate for the computation delay [28]. The current at instant $k+2$, instead of $k+1$.

$$\begin{cases} i_d(k+2) = \dfrac{T_s}{L_d} u_d(k+1) + (1 - \dfrac{R_s}{L_d} T_s) i_d(k+1) \\ +T_s \omega_e \dfrac{L_q}{L_d} i_q(k+1) \\ i_q(k+2) = \dfrac{T_s}{L_q} u_q(k+1) + (1 - \dfrac{R_s}{L_q} T_s) i_q(k+1) \\ -T_s \omega_e \dfrac{L_d}{L_q} i_d(k+1) - \dfrac{T_s \omega_e \psi_f}{L_q} \\ i_{01}(k+2) = \dfrac{T_s}{L_\sigma} u_{01}(k+1) + (1 - \dfrac{R_s}{L_\sigma} T_s) i_{01}(k+1) \end{cases} \tag{15}$$

Therefore, the cost function is expressed as

$$J = \left|i_d^* - i_d(k+2)\right| + \left|i_q^* - i_q(k+2)\right| + \lambda_2 \left|i_{01}^* - i_{01}(k+2)\right| \tag{16}$$

C. MODES INTEGRATED CONTROL

According to the overview of the operation modes, the DC charging and in-motion charging modes can be implemented by extending the control of normal driving. Given the abundance of control degrees of freedom present in a multi-phase drive system, the charging current control can be converted into the zero-sequence subspace current control. On the basis of that, the mode integrated control can be achieved by utilizing the enhanced dual-vector MPC, namely mode predictive current integrated control.

The proposed MPCIC shared for all operating modes is depicted in Fig. 6. The control diagram is mainly structured of seven components, namely decoupling transformation, speed control, reference values of 0_1-axis currents calculation, mode selection, predictive model control, cost function, and pulse generation. The MPCIC is implemented with the following steps:

1) *Step* 1. The six-phase machine phase currents are decoupled to the d-q subspace, x-y subspace, and the 0_1-axis by the utilization of the decoupling matrix $\mathbf{T}_{VSD}$ and the Park transformation matrix $\mathbf{T}_{\text{park}}$.
2) *Step* 2. Speed control is accomplished by employing a PI controller to accurately track the desired speed n^* and ensure proper operation in the normal driving and in-motion charging modes, while also maintaining the EV stationary during DC charging mode ($n^* = 0$) to support the charging process.
3) *Step* 3. The speed PI controller determines the reference of the q-axis current I_q^*, while the d-, x-, and y-axes current references are assigned to zero.
4) *Step* 4. The operating modes of EDROC are implemented by mode selection, with the corresponding mode switch being deactivated. Simultaneously, the reference value of the 0_1-axis current in the relevant mode is calculated.
5) *Step* 5. The reference value of the 0_1-axis current is calculated in the cases of DC grid, VRPPs and no source (i.e., without using grid or VRPPs) are connected, respectively. When no source is connected to machine neutral points, the system will operate in the normal driving mode and $I_{01}^* = I_{01\_1}^* = 0$. During the charging modes, the $I_{01}^* = I_{01\_2}^*$ when the DC grid is connected, while the minimum value between charging control and MPPT output ($I_{01\_2}^*$ and I_{PP}^*) is chosen as the 0_1–axis current reference ($I_{01\_3}^*$) when the VRPPs are connected.
6) *Step* 6. The predicted currents are calculated by the predictive model and inputted into the cost function

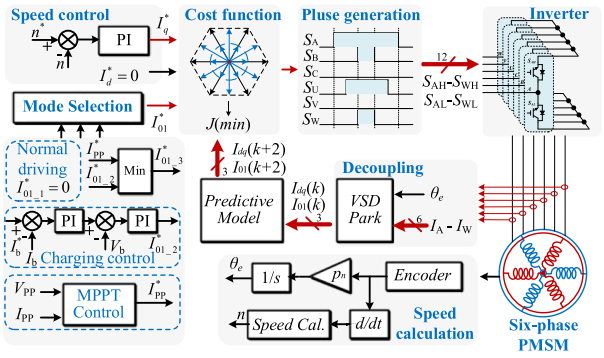

FIGURE 6. Block diagram of MPCIC.

along with the current reference value to determine the optimal voltage vector for the subsequent cycle.

7) *Step* 7. The switching state of the transistor is determined by the selected optimal vector, thereby facilitating the integrated control of various modes in the proposed system.

IV. EXPERIMENTAL VERIFICATIONS

To experimentally validate the feasibility and effectiveness of the proposed EDROC, an experimental prototype is established as shown in Fig. 7. The experimental prototype utilizes a 2kW six-phase symmetrical PMSM, with the key parameters listed in Table 4. Then, the load is generated by a magnetic powder brake. Two 36V/300W photovoltaic panels connected in series and a 3kW DC power supply with a maximum voltage of 100V are chosen to simulate the VRPPs and the emerging DC grid, respectively. Furthermore, a 144V/50AH lithium battery is selected as charging objection to verify the charging mode. The implementation of the enhanced MPC is carried out utilizing a digital signal processor (TMS320F28335). Finally, the six Infineon FF300R12ME4 insulated gate bipolar transistors (IGBTs) modules are employed to constitute the six-phase inverter. However, the operating frequency of the IGBTs is 10kHz due to constraints imposed by the experimental platform. Moreover, HCS-LTS3-15A current sensors and HVS-AS3.3-05mA voltage sensors are employed for current and voltage measurements respectively.

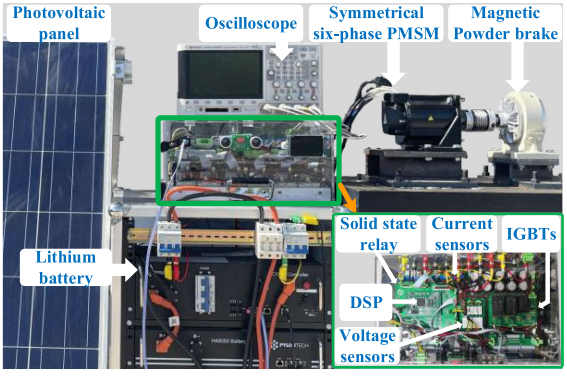

FIGURE 7. Experimental prototype.

TABLE 4. Main parameters of the EDROC.

Parameters	Values
Rated voltage (PMSM)	110V
Rated current (PMSM)	20A
Rated torque (PMSM)	9.5N·m
Rated power (PMSM)	2.0kW
Rated speed (PMSM)	2000rpm
Number of pole pairs	5
Direct axis inductance	5.56mH
Quadrature axis inductance	7mH
0-axis inductance	0.125mH
Phase resistance	0.3Ω
Stator-PM magnetic flux	0.042Wb
IGBTs frequency	10kHz
Battery voltage	144V
Battery capacity	50AH
Maximum charging current	25A
Charge cutoff voltage	156V

A. NORMAL DRIVING MODE

The performances of the normal driving mode, including machine phase currents (I_A and I_U), torque, speed, d–q, and x–y subspace currents under the desired speed of 500r/min in conjunction with 4N• m load, are shown in Fig. 8. It is readily evident that the machine phase currents are a significant disparity between the conventional MPC and the enhanced MPC. The machine phase currents are sinusoidal for the MPC scheme, while the current quality is significantly deteriorated in the conventional MPC scheme.

In principle, the primary factor impeding the current quality is the inadequate control of subspace currents, as demonstrated by comparing d–q and x–y subspace currents in two schemes. Additionally, both two schemes effectively track the d–q, and x–y subspace currents to ensure the stabilization around the reference. Nevertheless, the occurrence of higher ripple in the d–q and x–y subspace currents of the conventional MPC contributes to elevated torque ripple, which directly impacts the performance of application. In contrast, the enhanced MPC scheme effectively suppresses the harmonics of subspace currents, thereby maintaining the stability of the speed n and the output torque T_e. Furthermore, the enhanced MPC scheme not only minimizes operating noise but also mitigates losses and enhances security during operation compared to conventional MPC.

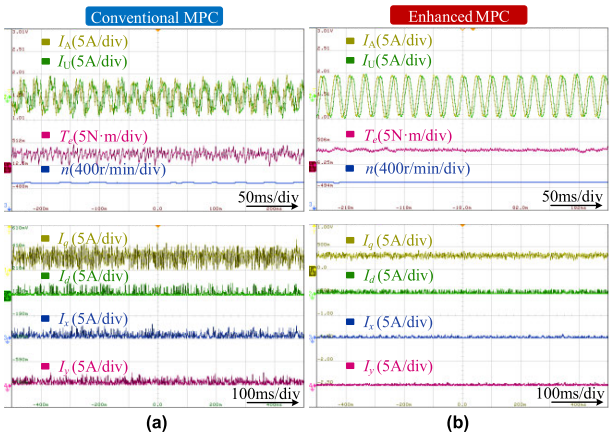

FIGURE 8. Normal driving performances. (a) Conventional MPC scheme. (b) Enhanced MPC scheme.

B. DC CHARGING MODE

The experimental results of DC charging are illustrated in Figs. 9-10, where the DC power supply is set at 100V. The steady-state experimental results of the DC charging mode for both conventional MPC and the enhanced MPC are depicted in Fig. 9, where the DC power supply is utilized. Concretely, the two schemes demonstrate the capability to accurately track charging current I_b of 2A, while maintaining

the observed charging voltage V_b of 150V. This fulfills the fundamental requirements for battery charging. Compared to the enhanced MPC scheme, the conventional MPC scheme exhibits higher ripple in both phase current (approximately 1A) and DC current (approximately 1.7A). The enhanced MPC scheme is further validated for its effectiveness in reducing harmonics and improving current tracking capability within the subspace. In addition, the amplitudes of each machine phase current are identical, signifying the generation of zero electromagnetic torque.

Apart from the analysis of steady-state performance, the transient-state response is also investigated by considering the saltus step of charging current, which is varied in a step manner from 2 to 3.5 A, as presented in Fig. 10. Exceptional tracking performance of charging current, along with the maintenance of a consistent charging voltage, can be observed. For both schemes, the sudden increase in the charging current has a minimal impact on the phase current and DC current. The enhanced MPC scheme not only ensures dynamic performance but also provides a significant improvement in steady-state performance.

Then, the experiment is carried out to compare the dynamic performances of enhanced MPC scheme and traditional vector control scheme. Fig. 11 corresponds to the charging current variation operation in a manner where the charging current alters from 2A to 3.5A. As seen, the response times of the enhanced MPC scheme are observed to be lower than that of the traditional vector control scheme, indicating that the enhanced MPC demonstrates superior dynamic performance.

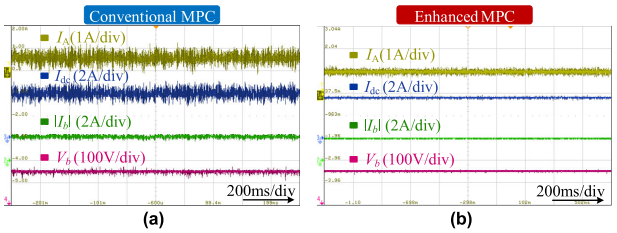

FIGURE 9. DC charging operation performances powered by DC source in steady-state. (a) Conventional MPC scheme. (b) Enhanced MPC scheme.

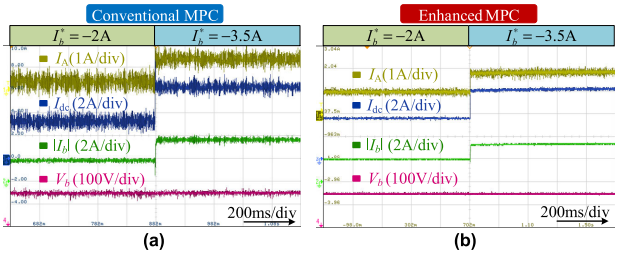

FIGURE 10. DC charging performances powered by DC source to a step in charging current from 2A to 3.5A. (a) Conventional MPC scheme. (b) Enhanced MPC scheme.

C. IN-MOTION CHARGING MODE

In the in-motion charging mode, the VRPPs are subjected to a condition of 1050W/m^2 and 25°C. Fig. 12 illustrates the

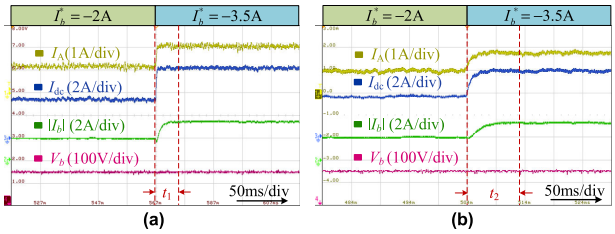

FIGURE 11. Dynamic performances of DC charging mode. (a) Enhanced MPC scheme. (b)Conventional vector control scheme.

experimental results of in-motion charging at a desired speed of 500r/min in conjunction with 4N• m load. The amplitudes of phase currents I_A and I_U are observed to be non-identical due to the injection of 0_1–axis current, which is attributed to the opposite effects exerted on the two sets of three-phase windings. In addition, the conventional MPC scheme exhibits a damnable waveform quality of phase currents, resulting in significant fluctuations in the electromagnetic torque and speed, thereby adversely affecting the overall driving performance. Meanwhile, the noticeable fluctuation in the charging current of the battery, as well as the output current and voltage of the VRPPs, also affects the charging performance of the system. Nevertheless, the phase currents maintain remarkable sinusoidal qualities, while concurrently ensuring stability in torque, speed, and charging current within the enhanced MPC scheme.

Undeniably, the performance of the system is intricately connected to the control of subspace currents. It can be inferred that the control effect of subspace currents is the primary factor that influences the system performance from the comparison in Fig. 12. In the conventional MPC scheme, the inadequate control of subspace current results in a higher ripple, resulting in elevated ripple torque and charging

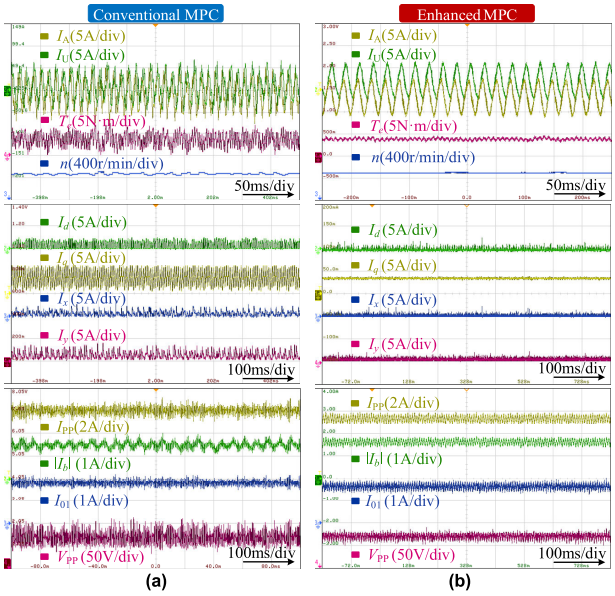

FIGURE 12. Experimental results of in-motion charging. (a) Conventional MPC scheme. (b) Enhanced MPC scheme.

current. Conversely, the enhanced MPC scheme restrains the harmonics within the subspace current, ensuring stability in the output torque and charging current, consequently yielding enhanced performance. Moreover, even if the portion of the x–y subspace is eliminated from the cost function, the ripple in x–y subspace currents can be decreased from 3.4A (with conventional MPC scheme) to 0.8A (with enhanced MPC scheme).

Moreover, the FFT results of I_A in the normal driving mode are depicted in Fig. 13. The total harmonic distortion (THD) of phase current in the normal driving mode with the conventional MPC scheme is about 40.88%, which is higher than that with the enhanced MPC scheme (5.24%). This distinction is primarily attributed to the subspace currents control. Additionally, the FFT results of I_A in the in-motion charging mode are depicted in Fig. 14. The THD of phase current in the in-motion charging mode with the conventional MPC scheme is about 42.93%, which is higher than that with the enhanced MPC scheme (14.70%). In contrast to the normal driving mode, the harmonic increases significantly in in-motion charging mode as a result of the unequal impedances of stator windings and composition of zero sequence space.

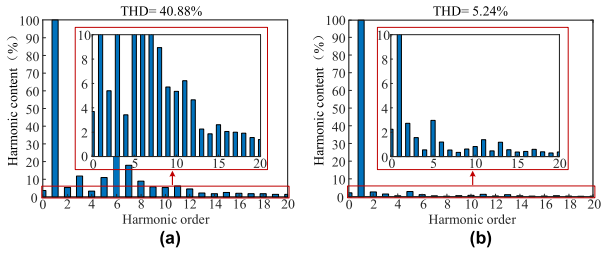

FIGURE 13. THD of I_A in normal driving mode under speed setting of 500r/min with 4N● m load. (a) Conventional MPC scheme. (b) Enhanced MPC scheme.

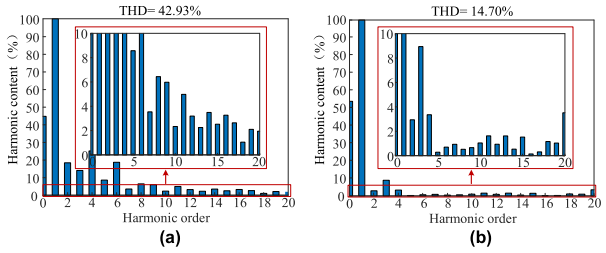

FIGURE 14. THD of I_A in in-motion charging mode under speed setting of 500r/min with 4N● m load. (a) Conventional MPC scheme. (b) Enhanced MPC scheme.

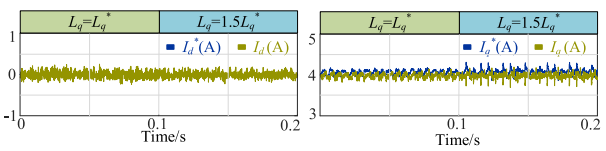

FIGURE 15. Experimental results of the enhanced MPC scheme with 50% inductance error.

Finally, to evaluate the parameter stability of the enhanced MPC scheme, the q-axis inductance is set as 150% of its nominal value. As depicted in Fig.15, although the mismatch that affects steady-state performance within the enhanced MPC scheme, it demonstrates commendable current-tracking performance both in the q-axis and d-axis. Overall, the enhanced MPC scheme demonstrates robustness against parametric uncertainties.

V. CONCLUSION

In the paper, the EDROC with the ability of DC charging, in-motion charging and normal driving for SPEV incorporating a six-phase machine is studied. The circuit topology of three operation modes and operation principles, especially the in-motion charging mode, of the EDROC are discussed in detail. After that, the MPCIC responsible for all operation modes is proposed, which makes the system control simpler and more reliable. Finally, the EDROC system with the MPCIC strategy is successfully verified by a 2-kW experimental prototype. According to the experiment results, the following conclusions are obtained:

1) To address the separate control of operation modes, the mode integrated control is designed in conjunction with the enhanced dual-vector MPC, enabling successful implementation of DC charging, in-motion charging, and normal driving by the MPCIC.
2) The DC charging and in-motion charging modes are implemented due to the driving and charging are controlled independently within the MPCIC scheme. In addition, the dedicated DC-DC converter between the VRPPs and the battery is eliminated in in-motion charging and DC charging modes, minimizing the supernumerary components.
3) Virtual vectors are investigated to effectively suppress harmonic currents in the three operation modes, and the THD of phase current in the normal driving and in-motion charging modes is diminished to 5.24% and 14.70%, respectively.

Although the feasibility of the proposed MPCIC strategy has been verified based on the experimental results; however, it is noteworthy that the realization of the multi-energy interface and the parameter adaptation in multi-mode will be the main focus of our future research.

REFERENCES

[1] S. S. G. Acharige, M. E. Haque, M. T. Arif, N. Hosseinzadeh, K. N. Hasan, and A. M. T. Oo, "Review of electric vehicle charging technologies, standards, architectures, and converter configurations," *IEEE Access*, vol. 11, pp. 41218–41255, 2023.

[2] S. Jaman, S. Chakraborty, D.-D. Tran, T. Geury, M. El Baghdadi, and O. Hegazy, "Review on integrated on-board charger-traction systems: V2G topologies, control approaches, standards and power density state-of-the-art for electric vehicle," *Energies*, vol. 15, no. 15, p. 5376, Jul. 2022.

[3] M. Tang, M. di Benedetto, S. Bifaretti, A. Lidozzi, and P. Zanchetta, "State of the art of repetitive control in power electronics and drive applications," *IEEE Open J. Ind. Appl.*, vol. 3, pp. 13–29, 2022.

[4] G. T. Chiang, T. Shuji, S. Takahide, Y. Hand, Y. Kitamura, and M. Fukada, "Coupled magnetic-based integrated isolated onboard battery charger and boost motor drive unit for electric vehicles," *IEEE Trans. Transport. Electrific.*, vol. 8, no. 1, pp. 135–148, Mar. 2022.

[5] H. Wouters and W. Martinez, "Bidirectional onboard chargers for electric vehicles: State-of-the-art and future trends," *IEEE Trans. Power Electron.*, vol. 39, no. 1, pp. 693–716, Jan. 2024.

[6] C. Viana, M. Pathmanathan, and P. W. Lehn, "Dual-inverter-integrated three-phase EV charger based on split-phase machine," *IEEE Trans. Power Electron.*, vol. 37, no. 12, pp. 15175–15185, Dec. 2022.

[7] H. J. Raherimihaja, Q. Zhang, T. Na, M. Shao, and J. Wang, "A three-phase integrated battery charger for EVs based on six-phase open-end winding machine," *IEEE Trans. Power Electron.*, vol. 35, no. 11, pp. 12122–12132, Nov. 2020.

[8] M. S. Rafaq, W. Midgley, and T. Steffen, "A review of the state of the art of torque ripple minimization techniques for permanent magnet synchronous motors," *IEEE Trans. Ind. Informat.*, vol. 20, no. 1, pp. 1019–1031, Jan. 2024.

[9] D. Thimmesch, "An SCR inverter with an integral battery charger for electric vehicles," *IEEE Trans. Ind. Appl.*, vol. IA-21, no. 4, pp. 1023–1029, Jul. 1985.

[10] X. Liu, F. Yu, J. Mao, and H. Yang, "Pre- and post-fault operations of six-phase electric-drive-reconstructed onboard charger for electric vehicles," *IEEE Trans. Transport. Electrific.*, vol. 8, no. 2, pp. 1981–1993, Jun. 2022.

[11] A. Salem and M. Narimani, "A review on multiphase drives for automotive traction applications," *IEEE Trans. Transport. Electrific.*, vol. 5, no. 4, pp. 1329–1348, Dec. 2019.

[12] M. Frikha, J. Croonen, K. Deepak, Y. Benômar, M. El Baghdadi, and O. Hegazy, "Multiphase motors and drive systems for electric vehicle powertrains: State of the art analysis and future trends," *Energies*, vol. 16, no. 2, p. 768, Jan. 2023.

[13] I. Subotic, N. Bodo, and E. Levi, "Single-phase on-board integrated battery chargers for EVs based on multiphase machines," *IEEE Trans. Power Electron.*, vol. 31, no. 9, pp. 6511–6523, Sep. 2016.

[14] I. Subotic, N. Bodo, E. Levi, M. Jones, and V. Levi, "Isolated chargers for EVs incorporating six-phase machines," *IEEE Trans. Ind. Electron.*, vol. 63, no. 1, pp. 653–664, Jan. 2016.

[15] N. Bodo, E. Levi, I. Subotic, J. Espina, L. Empringham, and C. M. Johnson, "Efficiency evaluation of fully integrated on-board EV battery chargers with nine-phase machines," *IEEE Trans. Energy Convers.*, vol. 32, no. 1, pp. 257–266, Mar. 2017.

[16] A. K. Singh, M. Badoni, and Y. N. Tatte, "A multifunctional solar PV and grid based on-board converter for electric vehicles," *IEEE Trans. Veh. Technol.*, vol. 69, no. 4, pp. 3717–3727, Apr. 2020.

[17] C. Viana and P. W. Lehn, "A drivetrain integrated DC fast charger with buck and boost functionality and simultaneous drive/charge capability," *IEEE Trans. Transport. Electrific.*, vol. 5, no. 4, pp. 903–911, Dec. 2019.

[18] F. Yu, Z. Zhu, X. Liu, and Z. Zhang, "Electric-drive-reconstructed onboard charger for solar-powered electric vehicles incorporating six-phase machine," *IEEE Trans. Power Electron.*, vol. 37, no. 6, pp. 6544–6555, Jun. 2022.

[19] F. Yu, Q. Yin, Z. Zhu, and X. Cheng, "A multienergy interface electric-drive-reconstructed onboard charger for EVs with integrated control strategy," *IEEE Trans. Power Electron.*, vol. 39, no. 4, pp. 4050–4061, Apr. 2024.

[20] B. Talbi, F. Krim, A. Laib, A. Sahli, and B. Babes, "A sugeno-fuzzy tuning approach of weighting factor in model predictive control for PV grid-tied PUC7 multi-level inverter," in *Proc. 3rd Int. Conf. Smart Grid Renew. Energy (SGRE)*, Mar. 2022, pp. 1–6.

[21] B. Babes, L. Rahmani, A. Chaoui, and N. Hamouda, "Design and experimental validation of a digital predictive controller for variable-speed wind turbine systems," *J. Power Electron.*, vol. 17, no. 1, pp. 232–241, Jan. 2017.

[22] Z. Zhang, Z. Wang, X. Wei, Z. Liang, R. Kennel, and J. Rodriguez, "Space-vector-optimized predictive control for dual three-phase PMSM with quick current response," *IEEE Trans. Power Electron.*, vol. 37, no. 4, pp. 4453–4462, Apr. 2022.

[23] F. Yu, X. Liu, Z. Zhu, and J. Mao, "An improved finite-control-set model predictive flux control for asymmetrical six-phase PMSMs with a novel duty-cycle regulation strategy," *IEEE Trans. Energy Convers.*, vol. 36, no. 2, pp. 1289–1299, Jun. 2021.

[24] S. Sharma, M. V. Aware, and A. Bhowate, "Symmetrical six-phase induction motor-based integrated driveline of electric vehicle with predictive control," *IEEE Trans. Transport. Electrific.*, vol. 6, no. 2, pp. 635–646, Jun. 2020.

[25] M. S. Abdel-Majeed, A. Shawier, A. Habib, A. S. Abdel-Khalik, M. S. Hamad, S. Ahmed, and N. A. Elmalhy, "A three-phase nonisolated pseudo-six-phase-based integrated onboard battery charger for electric vehicles," *IEEE Trans. Transport. Electrific.*, vol. 9, no. 1, pp. 1300–1310, Mar. 2023.

[26] R. A. Taha, W. E. Abdel-Azim, A. Shawier, and M. Y. Metwly, "Single-phase charging of six-phase integrated on-board battery charger using predictive current control," *IEEE Trans. Transport. Electrific.*, vol. 10, no. 1, pp. 540–552, Mar. 2024.

[27] Y. Hu, Z. Q. Zhu, and M. Odavic, "Comparison of two-individual current control and vector space decomposition control for dual three-phase PMSM," *IEEE Trans. Ind. Appl.*, vol. 53, no. 5, pp. 4483–4492, Sep. 2017.

[28] P. Cortes, J. Rodriguez, C. Silva, and A. Flores, "Delay compensation in model predictive current control of a three-phase inverter," *IEEE Trans. Ind. Electron.*, vol. 59, no. 2, pp. 1323–1325, Feb. 2012.

FENG YU (Member, IEEE) was born in Suzhou, China, in 1985. He received the B.Eng. degree in electrical engineering and automation from the School of Electrical Engineering, Sanjiang University, Nanjing, China, in 2008, the M.Sc. degree in electrical engineering from the School of Electrical and Information Engineering, Jiangsu University, Zhenjiang, China, in 2011, and the Ph.D. degree in electrical engineering from the Department of Electrical Engineering, Southeast University, Nanjing, in 2016. Since 2016, he has been with Nantong University, Nantong, China, where he is currently a Professor with the School of Electrical Engineering. His current research interests include the control of multiphase machines and drives for applications ranging from automotive to renewable energy.

QIHAO YIN was born in Xuzhou, China, in 2000. He received the B.Eng. degree from the School of Electrical Engineering, Nantong University, Nantong, China, in 2022, where he is currently pursuing the M.Sc. degree. His main research interest includes electric-drive-reconstructed onboard charging system along with multi-functional applications in solar electric vehicles.

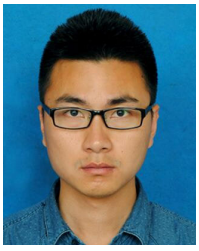

LAIWU LUO was born in Huaian, China, in 1987. He received the B.Eng. degree in electrical engineering and automation and the M.Sc. degree in control theory and control engineering from the School of Electrical Engineering, Nantong University, Nantong, China, in 2011 and 2014, respectively. Since 2014, he has been with Nantong University, where he is currently an Experimenter with the School of Electrical Engineering. His current research interests include motor drive and control technology, electric-drive-reconstructed onboard charger along with its application in electric vehicle, and new energy technology.

YUHAO ZHANG was born in Anqing, China, in 2000. He received the B.Eng. degree from the School of Electrical Engineering, Nantong University, Nantong, China, in 2022, where he is currently pursuing the M.Sc. degree. His current research interests include electromagnetic performance evaluation and analysis of electric-drive-reconstructed onboard charger.